photonics

MDPI

Article

Angle-Tunable Method for Optimizing Rear Reflectance in Fabry–Perot Interferometers and Its Application in Fiber-Optic Ultrasound Sensing

Yufei Chu [1,2,*], Mohammed Alshammari [1], Xiaoli Wang [1] and Ming Han [1]

[1] Department of Electrical and Computer Engineering, Michigan State University, East Lansing, MI 48825, USA; alsham19@msu.edu (M.A.); wangx250@msu.edu (X.W.); mhan@egr.msu.edu (M.H.)
[2] School of Marine and Atmospheric Sciences, Stony Brook University, Stony Brook, NY 11790, USA
* Correspondence: yufei.chu@stonybrook.edu

Abstract: With the introduction of advanced Fiber Bragg Grating (FBG) technology, Fabry–Pérot (FP) interferometers have become widely used in fiber-optic ultrasound detection. In these applications, the slope of the reflectance is a critical factor influencing detection results. Due to the intensity limitations of the laser source in fiber-optic ultrasound detection, the reflectance of the FBG is generally increased to enhance the signal-to-noise ratio (SNR). However, increasing reflectance can cause the reflectance curve to deviate from a sinusoidal shape, which in turn affects the slope of the reflectance and introduces greater errors. This paper first investigates the relationship between the transmission curve of the FP interferometer and reflectance, with a focus on the errors introduced by simplified assumptions. Further research shows that in sensors with asymmetric reflectance slopes, their transmittance curves deviate significantly from sinusoidal signals. This discrepancy highlights the importance of achieving symmetrical slopes to ensure consistent and accurate detection. To address this issue, this paper proposes an innovative method to adjust the rear-end reflectance of the FP interferometer by combining stress modulation, UV adhesive, and a high-reflectivity metal disk. Additionally, by adjusting the rear-end reflectance to ensure that the transmittance curve approximates a sinusoidal signal, the symmetry of the slope is maintained. Finally, through practical ultrasound testing, by adjusting the incident wavelength to the positions of slope extrema (or zero) at equal intervals, the expected ultrasound signals at extrema (or zero) can be detected. This method converts the problem of approximating a sinusoidal signal into a problem of the slope adjustment of the transmittance curve, making it easier and more direct to determine its impact on detection results. The proposed method not only improves the performance of fiber-optic ultrasound sensors but also reduces costs, paving the way for broader applications in medical diagnostics and structural health monitoring.

Keywords: Fabry–Pérot (FP); fiber Bragg grating; (FPI); fiber-optic ultrasound sensors; reflectance matching

Citation: Chu, Y.; Alshammari, M.; Wang, X.; Han, M. Angle-Tunable Method for Optimizing Rear Reflectance in Fabry–Perot Interferometers and Its Application in Fiber-Optic Ultrasound Sensing. *Photonics* **2024**, *11*, 1100. https://doi.org/10.3390/photonics11121100

Received: 28 October 2024
Revised: 14 November 2024
Accepted: 18 November 2024
Published: 21 November 2024

1. Introduction

Fabry–Perot interferometers (FPIs) are highly regarded for their exceptional sensitivity and precision, which form the backbone of numerous applications across both scientific and industrial domains. Their versatility is particularly evident in telecommunications, where FPIs play a crucial role in enhancing signal processing and data transmission over vast networks. By employing tunable optical filters, these devices facilitate dense channel analysis and effectively suppress optical noise, contributing significantly to the efficiency and reliability of modern communication systems [1,2]. This capability has become indispensable in the deployment of large-scale communication infrastructures, driving advancements in the telecommunications industry. In the realm of environmental monitoring, the acute sensitivity of FPIs to optical path variations allows for the precise detection of trace gasses and pollutants, which is critical for environmental protection and pollution control. When

integrated with Doppler technology, FPIs can provide wind field data over distances exceeding 100 km, which is vital for climate research and pollution management [3–6]. This application not only enhances our understanding of atmospheric dynamics but also supports sustainable environmental practices.

Moreover, the integration of FPIs with fiber Bragg grating (FBG) technology has led to significant advancements in fiber-optic sensing. By leveraging the stable optical properties within fiber-optics, FPIs enable highly accurate ultrasonic wave detection, thus expanding possibilities in both biomedical and environmental sensing applications [7,8]. These developments have not only improved sensor performance but have also opened up new avenues for high-precision measurements in various fields. Recent innovations include the development of high-sensitivity temperature sensors within FP cavities filled with ultraviolet glue, designed specifically for applications such as real-time ocean temperature monitoring [9–11]. Through continuous efforts, researchers have significantly improved the adaptability and precision of FPIs to maintain high accuracy and reliability in complex and demanding environments. For example, Wang et al. extended fiber-optic FPI technology to Raman lidar for atmospheric water vapor measurements [12,13]. Additionally, Karim et al. expanded the application of modified Phase-Generated Carrier (PGC) demodulation in the field of ultrasound detection [14]. Significant advancements have also been made in fiber-optic FPI temperature measurement techniques [15–17].

FBGs are typically produced through an ultraviolet (UV) light etching process, which causes periodic changes in the fiber's refractive index—essential for the reflective properties required by FP interferometers [15–17]. Increasing the reflectance causes the transmittance curve to gradually deviate from a sinusoidal shape. Although previous studies have shown that when the reflectance is within 26%, this deviation does not significantly impact the results [18], such findings are limited to specific applications. If the reflectivities of the two surfaces of the FPI are not properly selected, it may distort the slope of the reflectance spectrum. Such distortion can result in significant errors in the interferometer's response to ultrasound signals, thereby reducing the effectiveness of the detection system [16,18]. Therefore, a key challenge in optimizing FP interferometers for ultrasonic detection is ensuring that the reflectivities of the FBGs are precisely matched. This requires not only advanced manufacturing techniques but also rigorous testing and calibration. This paper takes a more general approach to FP fiber-optic systems, using the symmetry of the slope of the reflection spectrum as a metric to study the response to ultrasound signals.

This paper explores the fundamental principles of reflectivity in FP interferometers, focusing on how the reflectivity at both the front and back ends impacts the transmission rate and slope. We propose a novel method to adjust the rear reflectivity, which involves embedding a gold disk with UV adhesive at the fiber's rear. By manipulating the stress applied, the angle between the fiber rear face and the gold disk is adjusted, altering the reflectivity accordingly. Experimental results validate the feasibility and effectiveness of this approach. The implications of this research extend the functionality of fiber-optic ultrasonic sensors and, due to its cost-efficiency, broaden their potential applications in fields such as medical diagnostics, structural health monitoring, and non-destructive testing. This paper is structured as follows: Section 2 introduces the reflectance curves and slopes of Fabry–Pérot (FP) interferometers. Section 3 details the method of adjusting the reflectivity at the rear end to develop the FP sensor. Section 4 validates the results of ultrasound detection using the fabricated fiber-optic FP sensor. Finally, Section 5 provides a summary and discussion.

2. Reflectance Curves and Slopes of Fabry–Perot Interferometers

The transmission curve and its slope in FP interferometers are crucial for their performance in various detection applications and analytical tasks. At the core of an FP interferometer are two parallel, highly reflective surfaces. When light enters the interferometer, it undergoes multiple reflections between these surfaces. These repeated reflections cause the light beams to overlap, leading to constructive or destructive interference based

on several factors: the wavelength of the light, the angle at which the light enters the interferometer, and the separation between the mirrors, commonly referred to as the cavity length. To provide a clear and intuitive understanding of the transmission characteristics, we can examine a typical FP etalon used in Doppler lidar systems. An FP etalon generally consists of two parallel plates, which are usually made of materials such as glass or quartz. This configuration can also be adapted to feature two mirrors that serve as the reflective surfaces within an FP interferometer. Specifically, in the context of an etalon, the two parallel reflective surfaces are crucial components.

When a plane wave, represented as U_0, strikes the etalon, it undergoes a series of reflections and transmissions between these reflective surfaces. As depicted in Figure 1, the angle of incidence of U_0 is denoted by δ. The amplitude of the transmitted beam after these interactions can then be calculated, providing insights into the behavior of the system under specific conditions [19–21]. Assume the reflectivity of the front surface is R_1, the reflectivity of the rear surface is R_2, the refractive index between the two interfaces is n, and the thickness is h, the angle of incidence is denoted as θ. To visually represent the transmission curve and emphasize the importance of the reflective surfaces within the FP interferometer, this paper starts with the incident light and derives the formula for transmittance as follows [19]:

$$U_0' = U_0(1-R_1)(1-R_2) \tag{1}$$

$$U_1' = U_0(1-R_1)(1-R_2)R_1R_2e^{i\delta} \tag{2}$$

$$U_2' = U_0(1-R_1)(1-R_2)R_1^2R_2^2\,e^{2i\delta} \tag{3}$$

$$U_3' = U_0(1-R_1)(1-R_2)R_1^3R_2^3\,e^{3i\delta} \tag{4}$$

where $\delta = \frac{4\pi nh\cos\theta}{\lambda}$, and the total amplitude of the transmitted beam is

$$\begin{aligned} T &= \frac{U'U'^*}{U_0U_0^*} \\ &= \frac{(1-R_1)^2(1-R_2)^2}{(1-R_1R_2)^2+4R_1R_2\sin^2\left(\frac{\delta}{2}\right)} \end{aligned} \tag{5}$$

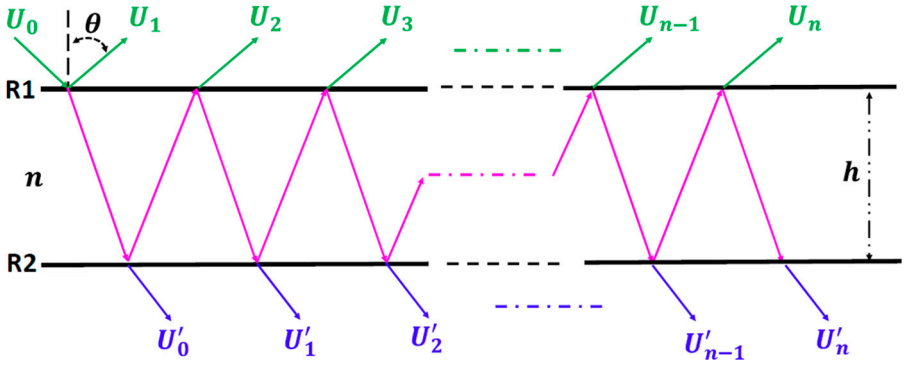

Figure 1. The schematic diagram of the FP transmittance curve.

Assuming that the reflectivity is low, and the amplitude reflectance of the two faces of the etalon are equal, that is, $R1 = R2$, the intensity reflectance of each face is as follows: $R = Ri^2$. In most current FBG applications, for the sake of computational simplicity, we typically assume that the reflectivity is very low and that the reflectivity of the two surfaces is identical. In this case, $(1 - Ri)^2$ is simplified to $(1 - Ri^2)$. In most applications, this simplification is reasonable and does not significantly affect the measurement results. However, in certain precise measurements, such as ultrasonic detection, this simplification can introduce errors. In practical applications, to enhance the detection signal without increasing the demand for higher incident laser power, people can increase the reflectivity of the sensor. However, while this increases the signal strength, it can also affect the

quality of the signal. Thus, it is crucial to understand how the relative error changes with reflectivity, as illustrated in Figure 2, which depicts the variation of errors in $(1 - Ri)^2$ and $(1 - Ri^2)$ with respect to reflectivity.

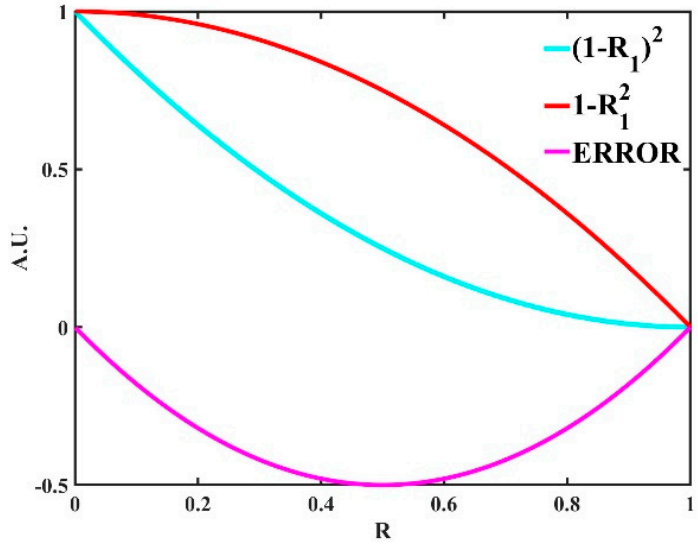

Figure 2. Variation of error due to assumptions in FP reflectivity changes.

As shown in Figure 2, the difference between the expected reflectivity and the measured reflectivity increases as reflectivity rises, reaching a peak at 50%, and then decreases as reflectivity continues to increase. This observed error trend must be considered in practical applications. Fortunately, in most applications, where reflectivity is less than 5%, the relative error, given by $1 - 0.05^2 - (1 - 0.05)^2 = 0.095$, is negligible and can be ignored. In practical applications, understanding the transmission curve of the FP interferometer allows us to determine whether the errors are within an acceptable range for detection when the FP is used as a filter, frequency discriminator, etc. [20].

In the field of fiber-optic ultrasonic detection, improving sensitivity is a key objective. To this end, the Han group pioneered a coiled fiber configuration that significantly enhances the signal-to-noise ratio (SNR) [14,22]. This innovative setup requires the use of longer FP cavity lengths, which reduce the full width at half maximum (FWHM) and necessitate highly stable laser wavelengths for optimal performance. The most common approach involves laser frequency stabilization; however, this method is typically expensive, limiting its application range. To address this, Han and colleagues developed additional strategies to mitigate the impact of laser wavelength drift, ensuring that ultrasonic detection remains stable and reliable even as laser wavelengths fluctuate with environmental changes [14,22]. These strategies are based on the assumption that $(1 - Ri)^2 = (1 - Ri^2)$. However, as shown in Figure 2, these assumptions may introduce a certain degree of error. The response in ultrasound detection is not only related to Figure 2 but also relies on a fundamental assumption that the transmittance curve is sinusoidal [14,18]. While it is generally assumed that lower reflectance is better, there is no specific metric to evaluate the extent of error caused by deviations in the reflectance curve. Therefore, this paper uses the slope of the reflectance to visually represent the error and further investigates how the slope affects the detection results.

To minimize the impact of this error, this paper conducts an in-depth study of the principles behind FBG ultrasound detection. When ultrasound waves pass through the FBG sensor, they cause slight changes in the refractive index, resulting in a phase shift (or a change in the relative position of the laser wavelength to the transmission curve). The detection sensitivity is directly related to the slope; the steeper the slope, the higher the sensitivity. The actual detected signal is the product of the reflectance curve and the

reflected light intensity. For simplification, this discussion initially considers only the intensity changes caused by slope variations.

However, with changes in reflectance, the assumption of a sinusoidal shape for the transmittance curve may no longer hold. As shown in Figure 3, variations in reflectance can lead to significant deviations of the transmittance curve from a sinusoidal shape, thereby affecting the accuracy and reliability of the detection process. In Figure 3a, when $R1 = R2 = 1\%$, the reflectance curve is nearly sinusoidal, and its slope is almost symmetrical. However, when the reflectance increases to 30%, it is evident that the reflectance curve is no longer sinusoidal, and its slope is no longer symmetrical. As the reflectance continues to rise, the asymmetry of the slope and the deviation of the transmittance curve from the sinusoidal shape become more pronounced. It is important to note that in Figure 3, for ease of comparison of slopes at different reflectance levels, each transmittance curve and its corresponding slope have been normalized by dividing by their respective maximum values. This normalization allows for a clearer comparison of how the shape and steepness of the curves change with varying levels of reflectance. Since the slope of the reflectance more directly impacts the detection signal, we will subsequently focus on the slope of the transmittance curve.

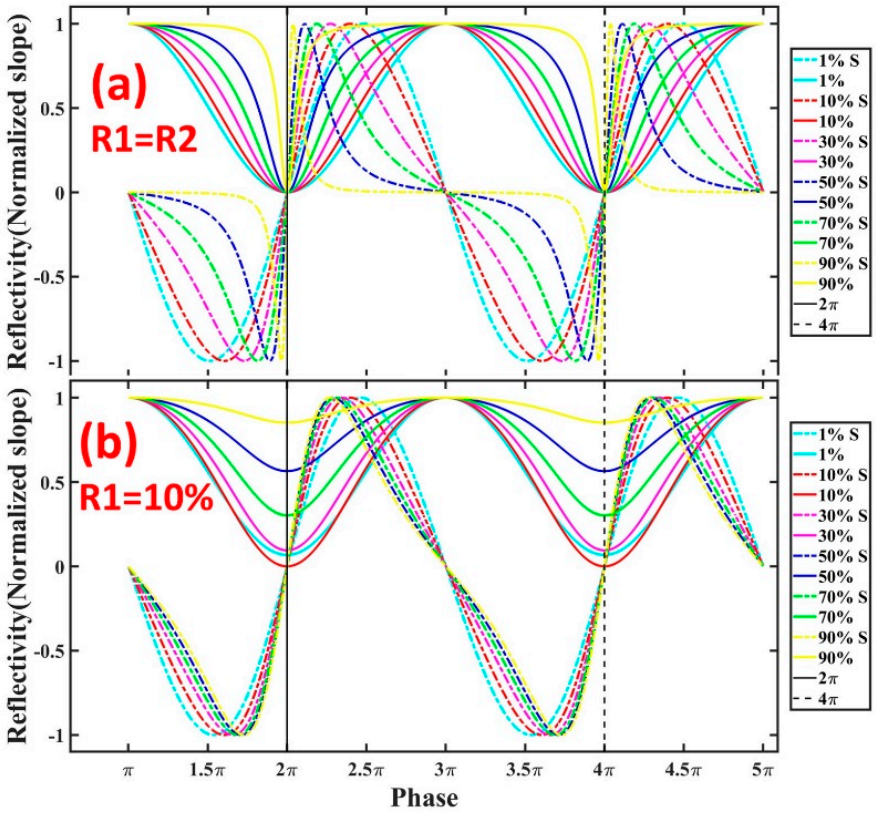

Figure 3. The variation in the slope due to the FP reflectivity changes. (**a**) The reflectivity of the front and rear ends is equal; (**b**) the reflectivity of the front end is fixed at 10%, and only the reflectivity of the rear end is changed; the solid line is the reflectivity; the dotted line is the slope of the normalized reflectivity. In the legend, "S" represents the slope.

When $R1$ and $R2$ are not equal, the slope of the reflectivity curve increases with the difference between the reflectivities. As shown in Figure 3b, we fixed $R1 = 10\%$ while varying $R2$. When $R1$ has a reflectivity of 10%, the optimal reflectivity of $R2$ is determined by the application scenario. In general applications, choosing R2 with a reflectivity of 10% is preferable. However, when considering the introduction of an additional light path or phase-modulated incident light to mitigate wavelength drift, as in the phase-generated carrier demodulation scheme in [18], it is necessary to assume that the reflectivity curve

is sinusoidal, with a symmetric slope. If *R*2 is set to 10%, the reflectivity curve may deviate from the sinusoidal shape, and the asymmetry of the slope can clearly indicate the extent of deviation. By comparing the slope curves in Figure 3b, we can see that choosing R2 at 1% is more suitable in this context. The figure demonstrates that when *R*2 = 1%, the reflectivity slope is most symmetric. However, as *R*2 increases, the slope becomes increasingly asymmetric. It is important to note that in Figure 3a, where *R*1 = *R*2, all the reflectivity curves reach the minimum of zero. However, as illustrated in Figure 3b, the reflectivity curve only reaches zero when both *R*1 and *R*2 are set to 10%; in all other cases, it does not. This characteristic is particularly advantageous for certain practical applications, such as when the backend detection component includes an envelope detector. Since it requires a specific operating threshold, it is preferable that the reflectivity does not drop to zero.

Based on the above analysis, it is clear that in ultrasound detection applications using FP sensors, such as those employing enhanced phase-generated carrier demodulation techniques [14], it is essential to assume that the reflectance curve is sinusoidal, with the transmittance slope being approximately linear and symmetrical. Satisfying this assumption is crucial to ensuring that one laser wavelength is positioned at the midpoint of the slope while another wavelength is at the peak or trough, regardless of frequency (phase) shifts. Symmetrical slopes are the foundation for maintaining the accuracy of this setup. However, as shown in Figure 3, deviations from these ideal conditions often occur. Variations in reflectance between the front and rear surfaces of the sensor can lead to changes in the transmittance curve and its slope. Specifically, as illustrated in Figure 3a, lower reflectance tends to result in more symmetrical slopes. However, achieving lower reflectance requires the use of higher laser energy. Figure 3b further demonstrates that the mismatch in reflectivity between the front and rear reflective surfaces of the FP (due to different reflectivities) results in distinct overall reflection curves and slopes.

3. Angle Adjustment of End-Face Reflectivity Based on UV Glue and Gold Disk

The results discussed in the previous section require the transmittance curve to have symmetrical slopes. According to the findings in Figure 3, this necessitates precise matching of the reflectance between the front and rear surfaces of the FP sensor. If only R1 uses the FPI, modifying *R*2 from an FPI to a gold disk can be used to adjust the reflectivity of *R*2. This is achieved by altering the angle of *R*2 (gold disk) to control the proportion of light reflected into the fiber, thereby adjusting *R*2's reflectivity. The reflectivity curves at different *R*2 settings are illustrated by the solid line in Figure 3b. Note that the final angle should be determined based on real-time monitoring of the reflectivity curve. Adjusting the reflectance of the FPI typically involves techniques such as XCL UV etching. However, as the demand for higher precision increases, so does the cost [20]. To accurately control reflectance while reducing manufacturing costs, we introduce an innovative method. Initially, the front FPI is created using XCL UV etching to establish *R*1. Then, depending on specific detection requirements, the reflectance *R*2 is adjusted at a specific length behind R1 to meet these requirements. This is achieved by fixing a gold disk (or other high-reflectivity material) at the fiber end with UV adhesive and adjusting the angle between the gold disk and the fiber end before UV curing. The detailed manufacturing process is as follows:

(1) Initial FPI creation: Using XCL UV etching, a front FPI is fabricated with the desired reflectivity R1. The fiber is positioned within the XCL optical path, and by carefully controlling the power and exposure time of the XCL laser, the reflectivity R1 can be precisely adjusted. It is important to note that the outcomes of this process can vary depending on the specific XCL optical setup and the material properties of the fiber. Therefore, after laser etching, it is essential to accurately measure and record the reflectivity of the FPI. This ensures that the fabricated FPI meets the required specifications and allows for any necessary adjustments in subsequent manufacturing steps [17].

(2) The preparation of the end side of fiber: Based on the specific requirements of the sensor, the fiber end face is carefully polished at a precise location behind R1. This ensures a smooth and flat surface that is essential for achieving the desired reflectivity. The fiber is then securely positioned on a three-dimensional translation stage using a fiber holder. This setup allows for precise alignment and positioning of the fiber end face, which is critical for the subsequent attachment of the reflective material. The accurate positioning ensures that the final reflectivity meets the specific sensor requirements, thereby optimizing the sensor's overall performance.

(3) Alignment: Place the gold disk on a three-dimensional moving platform and align the fiber using electron microscopy to ensure precise and gentle contact with the gold disk. The gold disk (reflector) needs to be larger than the fiber diameter but not excessively so to prevent detachment. As a compromise, we selected a reflector with a diameter of 600 μm.

(4) Reflectivity adjustment: Apply 0.5 mL of UV glue to the center of the gold disk using a syringe or micropump, then adjust the stress to modify the fiber's angle relative to the disk. Continuously monitor the transmission rate curve and fine-tune the stress (angle) to achieve the desired specifications. The adjustment range of the gold disk (reflector) is theoretically from 0 to the reflectivity of the gold disk (~90%), which fully meets our required range of adjustment.

(5) UV curing: solidify the configuration using a UV lamp to permanently set the angle between the fiber and the gold disk [16].

The results demonstrate that by continuously adjusting the angle, the sensor's slope can be effectively fine-tuned. When the slope becomes symmetrical, the reflectance curve closely approximates a sinusoidal signal, making it suitable for subsequent ultrasound detection. Figure 4a,b present the experimentally measured reflectance values and their corresponding slopes. In Figure 4a (highlighted in orange), the slope exhibits asymmetry, indicating that the reflectance curve can no longer be approximated as sinusoidal. In contrast, the slope (orange) in Figure 4b shows a high degree of symmetry, and the reflectance curve can be considered approximately sinusoidal. At this point, the FP sensor with symmetrical slopes can be used for ultrasound detection, which is applicable in phase-generated carrier (PGC) demodulation systems [14] or other FP-based detection applications that require a transmittance curve approximating a sinusoidal shape [23].

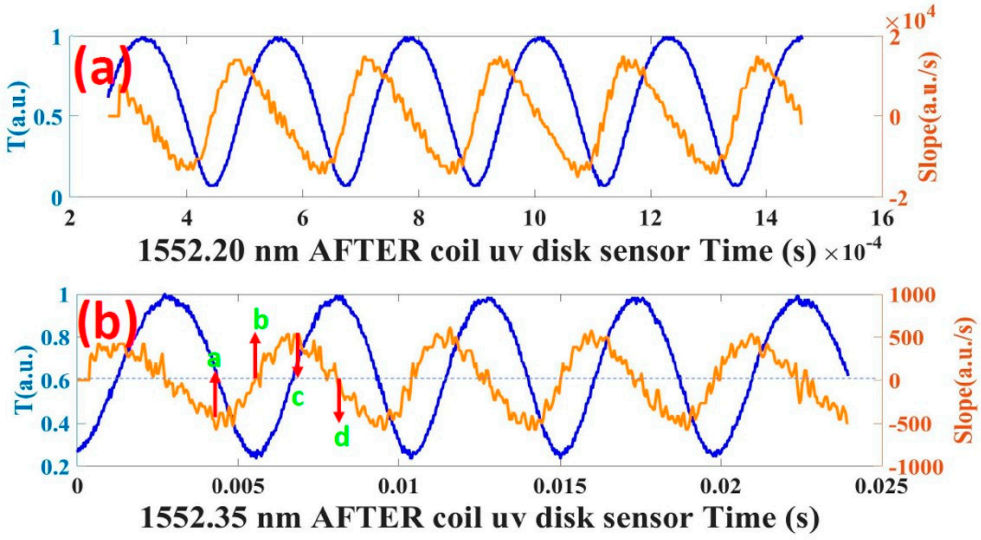

Figure 4. The angle adjustment of end−face reflectivity based on UV Glue. (**a**) The slope of the reflectivity is asymmetric; (**b**) the slope of the reflectivity is symmetric (the green points labeled a, b, c, and d correspond to the positions where the slope is at a minimum, zero, maximum, and zero, respectively).

Using a high-reflectivity metal disk at the back end can significantly expand the usable wavelength range of the fiber-optic FP sensor. When the transmittance of both the front FPI and the back-end FPI varies with wavelength, the range of incident laser wavelengths that meet detection requirements is greatly reduced. However, in the method proposed in this paper, the back-end reflectance can be approximately considered independent of wavelength, meaning only the front-end FPI varies with wavelength. This approach can significantly expand the working range of laser wavelengths. In the experiment, we used a piezoelectric transducer to precisely adjust the incident laser wavelength. We observed that since the reflectance of the front FPI varies with wavelength, this corresponds to R2 being fixed while R1 varies with wavelength, as shown in Figure 4. Figure 4a,b illustrate the changes in reflectance and its slope with varying laser wavelengths.

4. Results

To evaluate the actual performance of the FP ultrasound sensor, an FP ultrasound sensing system was set up as shown in Figure 5a. Both the fiber-optic FP sensor and the piezoelectric transducer were mounted on an aluminum plate, 25 cm apart. We utilized a Chirped Fiber Bragg Grating (CFBG) [17] to extend the operating wavelength of the first reflective surface to 1550 $\pm$ 5 nm. This system is designed to detect ultrasound waves generated by a piezoelectric transducer driven by a waveform generator, using the aforementioned fiber-optic FP sensor. The laser beam from the laser source is connected to port 1 of the circulator, with port 2 connected to the FP ultrasound sensor. The collected signal is then amplified by 40 dB using a photodetector (NEWPORT 1811-FC) connected to port 3 of the circulator, followed by a low-pass filter (500 kHz), and then fed into an oscilloscope (OSC, RIGOL DS1104B) or data acquisition card (DAQ). The fiber-optic FP sensor has a length of 38.97 cm and is coiled between R1 and R2 to form a disk with an inner diameter of approximately 6 mm and an outer diameter of approximately 8 mm [18]. The FP sensor is then fixed onto the aluminum plate using glue. The waveform generator produces a 150 kHz, 5 V peak-to-peak, five-cycle burst sinusoidal signal with a repetition rate of 40 Hz to drive the piezoelectric transducer and generate ultrasound waves.

The results demonstrate that sensors with good slope symmetry achieve the expected experimental outcomes. Figure 4a,b show the actual measured reflectance values and their corresponding slopes. It is evident that the slope in Figure 4a (indicated in orange) exhibits asymmetry, while the slope in Figure 4b shows a high degree of symmetry. For wphen the incident wavelength is adjusted to positions a, b, c, and d in Figure 4b, the corresponding results are shown in Figure 5b–e. When the laser wavelength is at the minimum value (position a), the detected signal strength is at a maximum. Similarly, when the laser wavelength is at the maximum value (position c), the detected signal strength is also at a maximum. When the laser wavelength is at points where the slope is zero (positions b and d), the ultrasound signal is zero. These experimental results exhibit strong symmetry. The four laser wavelengths in Figure 4b are equally spaced, with the slope exhibiting odd symmetry at points b and d, and even symmetry at points a and c. However, when using the sensor shown in Figure 4a, the intervals between the maxima and minima lack any symmetry.

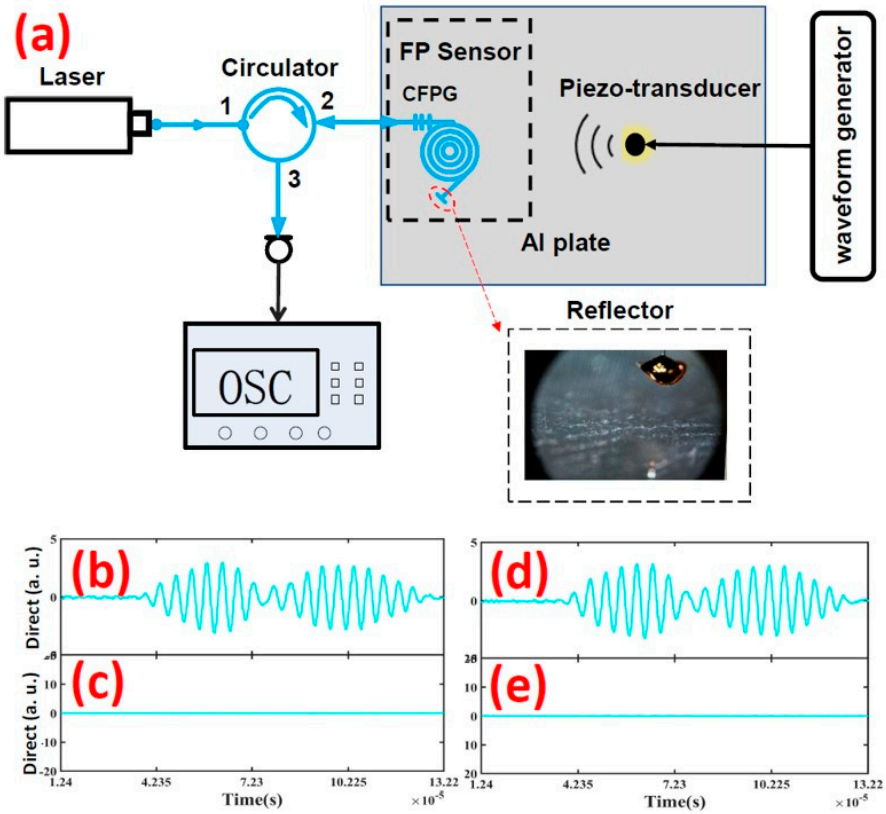

Figure 5. Angle symmetry testing setup and results for the ultrasound sensor: (**a**) ultrasound detection setup (the structure diagram of the FP sensor is shown within the black dashed line), (**b**−**e**) show the ultrasound detection results when the laser wavelength is adjusted to operating points a, b, c, and d in Figure 4b, respectively.

5. Conclusions and Discussion

This paper investigates the relationship between the transmission curve of the FP interferometer and reflectance, identifying potential errors introduced by simplified assumptions. It further examines the effects of asymmetrical slopes when the assumption of a sinusoidal transmittance curve is not met, which can significantly influence detection accuracy. To address this issue and achieve symmetrical slopes in the transmittance curve, this study proposes an innovative method for adjusting the back-end reflectance of the FP interferometer. This is accomplished through a combination of stress modulation, UV adhesive, and a high-reflectivity metal disk (gold disk). The effectiveness of the proposed method was validated through practical ultrasound detection experiments, which demonstrated improved symmetry in the detection results. This research offers a more cost-effective detection approach, potentially expanding the applicability of this technology. The results indicate that the detected signal strength reaches its maximum when the laser wavelength is at the slope's minimum (position a) and maximum (position c), while the ultrasound signal is zero at points where the slope of the transmittance curve is zero (positions b and d).

This paper comprehensively investigates the relationship between reflectance, transmittance, and the slope of the FP transmission curve, and introduces a cost-effective method for adjusting the end-face reflectance by modifying the angle between the fiber end face and a metal disk. Although a metal (gold) disk was used in this study, other similar reflective materials could potentially yield comparable results. The back-end reflectance is not wavelength-selective, which significantly broadens the usable wavelength range of the laser. The next step is to apply this FP sensor with the symmetric slope to practical scenarios where environmental interference can be mitigated (e.g., using a PGC scheme with an electro-optic modulator (EOM) or a dual-path approach with an acousto-optic modulator (AOM)) and to further compare its SNR performance. Future work could explore

fixing the angle between the metal disk and the fiber end face, and utilizing a CO_2 laser or femtosecond laser to etch the fiber to achieve the desired reflectance. This approach offers an additional means for fine-tuning reflectance, further enhancing the flexibility and applicability of sensor technology. The degree to which the reflectivity–transmittance curve deviates from a sinusoidal shape is often difficult to assess intuitively. However, in this paper, we propose using the slope of the reflectivity as a more intuitive metric to evaluate the extent of this deviation. This method can also serve as an indicator for evaluating how much the FP transmittance curve deviates from a sinusoidal shape in subsequent analyses. While this method was initially developed to adjust reflectance based on slope symmetry, it is equally applicable to general fiber-optic FP sensors without symmetry requirements [23], offering the potential to substantially reduce manufacturing costs while expanding the operating wavelength range.

Author Contributions: Conceptualization, Y.C.; methodology, Y.C.; software, Y.C.; data curation, Y.C. and X.W.; writing—original draft preparation, Y.C. and M.A.; writing—review and editing, M.H.; visualization, Y.C.; supervision, M.H.; project administration, M.H.; funding acquisition, M.H. All authors have read and agreed to the published version of the manuscript.

Funding: This research was funded by the Office of Naval Research (N000142112273, N000142212321).

Institutional Review Board Statement: Not applicable.

Informed Consent Statement: Not applicable.

Data Availability Statement: The data underlying the results presented in this paper are not publicly available at this time but may be obtained from the authors upon reasonable request.

Acknowledgments: Y. Chu would like to thank Hasanur Rahman Chowdhury for his help with the sensor fabrication and Qiwen Sheng for the technical discussion on FP modeling.

Conflicts of Interest: The authors declare no conflicts of interest.

References

1. Javernik, A.; Donlagic, D. High-speed interrogation of low-finesse Fabry–Perot sensors using a telecom DFB laser diode. *J. Light. Technol.* **2017**, *35*, 2161–2171. [CrossRef]
2. Moradi, H.; Zhoulideh, M.; Ghafariasl, M. Tunable and ultrasensitive sensor covering terahertz to telecommunication range based on a Fabry–Perot interference of graphene plasmonic waves. *Opt. Commun.* **2023**, *542*, 129592. [CrossRef]
3. Tan, L.; Hua, D.; Wang, L.; He, T.; Wang, Y.; Xing, M. Performance comparison of Fabry–Perot and Mach–Zehnder interferometers for molecular Doppler lidar based on fringe-imaging technique. *Optik* **2014**, *125*, 6291–6295. [CrossRef]
4. Chu, Y.; Liu, D.; Wang, Z. Basic principle and technical progress of Doppler wind lidar. *Chin. J. Quantum Electron.* **2020**, *37*, 580.
5. Chu, X.; Chen, Y.; Cullens, C.Y.; Yu, Z.; Xu, Z.; Zhang, S.R.; Huang, W.; Jandreau, J.; Immel, T.J.; Richmond, A.D. Mid-latitude thermosphere-ionosphere Na (TINA) layers observed with high-sensitivity Na Doppler lidar over Boulder (40.13° N, 105.24° W). *Geophys. Res. Lett.* **2021**, *48*, 2021GL093729. [CrossRef]
6. Zhao, M.; Chen, J.; Xie, C.; Li, L. The impacts of deformed Fabry–Perot interferometer transmission spectrum on wind lidar measurements. *Remote Sens.* **2024**, *16*, 1076. [CrossRef]
7. Domingues, M.F.; Tavares, C.; Alberto, N.; Radwan, A.; André, P.; Antunes, P. High rate dynamic monitoring with Fabry–Perot interferometric sensors: An alternative interrogation technique targeting biomedical applications. *Sensors* **2019**, *19*, 4744. [CrossRef] [PubMed]
8. Liu, B.; Li, Y.; Wang, R.; Chen, X.; Li, J.; Chen, H.; Jiang, M. Label-free and selective heparin detection by surface functionalized fiber Fabry-Perot interferometer biosensor. *Opt. Fiber Technol.* **2024**, *84*, 103770. [CrossRef]
9. Zhang, S.; Mei, Y.; Xia, T.; Cao, Z.; Liu, Z.; Li, Z. Simultaneous measurement of temperature and pressure based on Fabry-Perot interferometry for marine monitoring. *Sensors* **2022**, *22*, 4979. [CrossRef] [PubMed]
10. Han, G.L.M.; Hou, W. Fiber-Optic Temperature and Flow Sensor System and Methods. Patent US9995628B1, 12 June 2018. Available online: https://patents.google.com/patent/US9995628B1/en (accessed on 27 October 2024).
11. Liu, G.; Han, M.; Hou, W.; Matt, S.; Goode, W. A miniature fiber-optic sensor for high-resolution and high-speed temperature sensing in ocean environment. *Proc. SPIE* **2016**, *9459*, 80–85.
12. Wang, Y.; Jia, L.; Li, X.; Fan, F.; Di, H.; Song, Y.; Hua, D. Compact fiber-optic spectroscopic design and its validation in atmospheric water vapor Raman lidar. *J. Opt. Soc. Am. B* **2020**, *37*, 384944. [CrossRef]
13. Wang, Y.; Wang, Q.; Hua, H.D. Preliminary exploration of atmospheric water vapor, liquid water, and ice water by ultraviolet Raman lidar. *Opt. Express* **2019**, *27*, 36311–36321.

14. Karim, F.; Zhu, Y.; Han, M. Modified phase-generated carrier demodulation of fiber-optic interferometric ultrasound sensors. *Opt. Express* **2021**, *29*, 432237. [CrossRef]
15. Uddin, N.; Sheng, Q.; Lee, S.; Reinke, M.L.; Donovan, D.; Shafer, M.; Han, M. Multichannel fiber-optic silicon Fabry–Pérot interferometric bolometer system for plasma radiation measurements. *Photonics* **2021**, *8*, 344. [CrossRef]
16. Jiang, X.; Duan, Z.; Xu, T.; Mupfukirei, L.R.; Yu, Z.; Pang, B.; Wang, Y.; Ling, Q.; Chen, H.; Gu, Z.; et al. Review of fabrication and packaging of UV-induced FBGs for high temperature sensing. *Opt. Fiber Technol.* **2024**, *86*, 103855. [CrossRef]
17. Chowdhury, H.R. Fiber Optic Fabry-Pérot Interferometric Sensor for Temperature and Strain Measurement. Ph.D. Thesis, Michigan State University, East Lansing, MI, USA, 2023.
18. Karim, F.; Han, M. Effect of three-beam interference on phase-generated carrier demodulation of a fiber-optic interferometric sensor. *Opt. Express* **2023**, *31*, 9769–9778. [CrossRef] [PubMed]
19. Wang, Y.; Chu, Y.; Liu, D.; Wu, D.; Zhenzhu, W.A.; Kunming, X.I.; Kuang, Z.; Bangxin, W.A.; Zhong, Z.; Aiyuan, F.A.; et al. Device for Measuring Transmittance Curve of Fabry-Perot Using Frequency Comb Light Source and Method Using the Same. Patent US11874169B2, 16 January 2024. Available online: https://patents.google.com/patent/US11874169B2/en (accessed on 27 October 2024).
20. Sengupta, D. *Optical Fiber Sensors*; CRC Press: Boca Raton, FL, USA, 2015.
21. Chu, Y. Research on Technology and Method of Detecting Boundary Layer Parameters Based on Various Lidars. Ph.D. Thesis, University of Science and Technology of China, Hefei, China, 2020.
22. Liu, G.; Zhu, Y.; Sheng, Q.; Han, M. Polarization-insensitive, omnidirectional fiber-optic ultrasonic sensor with quadrature demodulation. *Opt. Lett.* **2020**, *45*, 397955. [CrossRef] [PubMed]
23. Alshammari, M.; Chu, Y.; Han, M. Real-time in-situ phase sensitivity calibration of interferometric fiber-optic ultrasonic sensors. *Opt. Lett.* **2024**, *49*, 5336–5339. [CrossRef] [PubMed]